

Nonlinear finite element analysis of lattice core sandwich beams

Praneeth Nampally^a, Anssi T. Karttunen^{a,b,*}, J.N. Reddy^a

^aTexas A&M University, Department of Mechanical Engineering, College Station, TX 77843-3123, USA

^bAalto University, Department of Mechanical Engineering, FI-00076 Aalto, Finland

Abstract

A geometrically nonlinear finite element model is developed for the bending analysis of micropolar Timoshenko beams using the principle of virtual displacements and linear Lagrange interpolation functions. The nonlinearity enters the model via a nonlinear von Kármán strain term that allows the micropolar beam to undergo moderate rotations. The nonlinear micropolar Timoshenko beam is used as an equivalent single layer model to study four different lattice core sandwich beams. A two-scale energy method is used to derive the micropolar constitutive equations for web, hexagonal, Y-frame and corrugated core topologies. Various bending cases are studied numerically using the developed 1-D finite element model. Reduced integration techniques are used to overcome the shear and membrane locking. The present 1-D results are in good agreement with the corresponding 2-D finite element beam frame results for global bending.

Keywords: Micropolar beam, Constitutive modeling, Geometric nonlinearity, Lattice material, Finite element, Nonlinear bending

1. Introduction

A typical sandwich panel consists of a thick, low-stiffness core between two relatively thin but stiff face sheets. The face sheets take bending and in-plane loads while the core carries transverse shear loads (Allen, 1969; Vinson, 1999). The face sheets and core can be made of the same or different materials and some possible core structures include, for example, foam, solid, honeycomb, and truss cores (Vinson, 2001). A number of manufacturing techniques are available for sandwich panels (Karlsson and Åström, 1997; Wadley et al., 2003). A sandwich panel generally has a high bending stiffness compared to a single solid plate of the same dimensions made of either the face sheet or core material and the panel weighs considerably less than the solid plate making it a weight-efficient structure (Vinson, 1999). Most early sandwich panels had isotropic face sheets but with the development of fiber reinforced composites, construction of sandwich panels with composite face sheets has become possible. Because of their high stiffness-to-weight ratios, structural efficiency and durability, sandwich panels are suitable candidates for high-speed aircraft and space applications (Schwingel et al., 2007). They have also found applications, for example, in shipbuilding (Kujala and Klanac, 2005; Roland and Metschkow, 1997) and other marine applications (Bitzer, 1994; Knox et al., 1998; Mouritz et al., 2001) and in the construction of bridges and buildings (Bright and Smith, 2004, 2007; Briscoe et al., 2011; Davalos et al., 2001; Nilsson et al., 2017).

Recompiled, unedited accepted manuscript. ©2019. Made available under [CC-BY-NC-ND 4.0](https://creativecommons.org/licenses/by-nc-nd/4.0/)

*Corresponding author. anssi.karttunen@iki.fi. **Cite as:** *Eur. J. Mech. A-Solid* 2019;160:66–75 [doi link](https://doi.org/10.1016/j.eurmech.2019.01.007)

The number of applications for sandwich panels is increasing rapidly. The required accuracy in the structural analysis of the panels depends on the type of the application considered. For example, in air-crafts a very detailed response of the sandwich structure may be required, whereas an overall global response may suffice in residential buildings when the natural vibration frequencies are of interest, for example. In any case, there is a need for appropriate modeling tools for different applications. Reviews on the modeling of sandwich structures have been given by several authors (Birman and Kardomateas, 2018; Carrera and Brischetto, 2009; Hohe and Librescu, 2004; Noor and Burton, 1995; Sayyad and Ghugal, 2017). Modeling methods for sandwich panels can be broadly classified as: (a) Complete 3-D analysis (computational or analytical), with complete details of the face sheets and the core structure considered; (b) layer-wise modeling with the faces and core considered as separate continuum layers (Reddy, 2004); (c) statically equivalent single layer (ESL) models. Although computational 3-D and layer-wise analyses give very detailed stress distributions for the panels, they come with the inherent disadvantage of including a large number of variables and, thus, the computational analysis of them can be very burdensome. Therefore, equivalent single layer theories such as the ESL first-order shear deformation (FSDT) beam and plate models are attractive especially when the global response of the structure is of main interest without accounting for every small detail. Extensive literature exists on the modeling of sandwich beam, plates and shells by ESL theories, see, for example (Abrate and Di Sciuva, 2017; Barut et al., 2002, 2001; Hohe and Librescu, 2004; Skvortsov and Bozhevolnaya, 2001).

It was shown recently that all-steel web-core sandwich beams deform so that when an ESL-FSDT model is used, the model has to take into account anti-symmetric shear deformations in order for the response of the sandwich structure to be captured accurately in some applications (Karttunen et al., 2018a). In more detail, the constituents of a 2-D or 3-D web-core sandwich beam model do not exhibit any anti-symmetric shear strains, but when the problem is reduced to a 1-D ESL beam problem essentially by thickness integration, the anti-symmetric behavior needs to be considered via a 1-D micropolar Timoshenko beam model. In this paper, we develop a geometrically nonlinear finite element model based on the micropolar Timoshenko beam theory.

With the revived interest in micropolar elasticity (Eringen and Suhubi, 1964), considerable work has been put into developing appropriate finite element models for micropolar continua in general; see, for example, (Li and Xie, 2004; Pothier and Rencis, 1994; Roman and Steinberg, 2013; Zhou and Cusatis, 2015). To list a few recent finite element models for micropolar plates we mention the works of Ansari et al. (2018, 2016) and Godio et al. (2014). Various finite element models have been proposed for the bending analysis of micropolar beams as well. Huang et al. (2000) used 3-D non-compatible finite elements to analyze the bending of beams, and Li and Xie (2004) proposed three different elements for plane micropolar elasticity and used them to analyze thin in-plane beams. Hassanpour and Hepler (2014) developed a 1-D micropolar beam finite element model using Lagrange interpolation functions. Regueiro and Duan (2015) derived a finite element model for a micropolar Timoshenko beam with the microrotation assumed to be equal to the cross-sectional rotation. More recently, Karttunen et al. (2018a) proposed nodally-exact 1-D finite element to analyze micropolar Timoshenko beams and Ansari et al. (2018) proposed a 27-node 3-D finite element for the analysis of beams. Only linear strains were considered in developing the finite element models in all the above mentioned papers.

In this study, in order to develop the geometrically nonlinear micropolar 1-D beam finite element, we start from the principle of virtual displacements and use the linear Lagrange interpolation functions. The originally linear micropolar Timoshenko beam model of Karttunen et al. (2018a)

is enriched by nonlinear von Kármán strains in order to account for the moderate rotations of the beam (Ding et al., 2016). Lattice cores, namely, hexagonal, corrugated and Y-frame cores in addition to the web-core topology studied earlier are considered. To this end, the two-scale constitutive modeling method presented by Karttunen et al. (2018b) is first generalized to cores other than the web-core.

In more detail, the rest of the paper is organized as follows. In Section 2, a brief review on the linear 1-D micropolar Timoshenko beam model is given followed by the two-scale constitutive modeling of the four different lattice cores after which the geometrically nonlinear micropolar Timoshenko beam equations are derived. In Section 3, the displacement based finite element model is formulated using the principle of virtual displacements. The element stiffness matrices are derived and the used nonlinear iterative procedures and techniques to avoid numerical locking are discussed. In Section 4, numerical examples are solved using the developed 1-D micropolar beam finite element model and are compared with the corresponding results from 2-D finite element analyses. Finally, concluding remarks are given in Section 5.

2. Geometrically nonlinear micropolar Timoshenko beam

Two-scale constitutive modeling of lattice materials in the context of linear micropolar Timoshenko beam theory is first carried out. The strain energy density for a geometrically nonlinear micropolar Timoshenko beam is obtained by retaining the linear constitutive matrix while the strain vector is augmented with von Kármán nonlinearity. The hyperelastic constitutive relations, i.e., the stress resultant equations for the nonlinear beam are derived from the strain energy for four lattice materials. The equilibrium equations for the nonlinear beam in terms of the stress resultants, and the corresponding weak form for finite element developments are attained by employing the principle of virtual displacements.

2.1. Displacements and linear strains

The two-dimensional displacements U_x and U_y and the independent microrotation Ψ of a micropolar Timoshenko beam can be written in terms of central axis kinematic variables as (Karttunen et al., 2018b)

$$U_x(x, y) = u_x(x) + y\phi(x), \quad U_y(x, y) = u_y(x), \quad \Psi(x, y) = \psi(x), \quad (1)$$

where u_x is the axial displacement, ϕ is the rotation of the cross-section, u_y is the transverse deflection, and ψ is the microrotation. The nonzero infinitesimal strains of the beam are

$$\begin{aligned} \varepsilon_x &= \frac{\partial U_x}{\partial x} = u'_x + y\phi' = \varepsilon_x^0 + y\kappa_x, & \kappa_{xz} &= \frac{\partial \Psi}{\partial x} = \psi' \\ \varepsilon_{xy} &= \frac{\partial U_y}{\partial x} - \Psi = u'_y - \psi, & \varepsilon_{yx} &= \frac{\partial U_x}{\partial y} + \Psi = \phi + \psi, \end{aligned} \quad (2)$$

where the prime “'” on the variables denotes differentiation with respect to x . The symmetric and anti-symmetric shear strains of the beam are defined as

$$\gamma_s = \varepsilon_{xy} + \varepsilon_{yx} = u'_y + \phi, \quad (3)$$

$$\gamma_a = \varepsilon_{xy} - \varepsilon_{yx} = u'_y - \phi - 2\psi = 2(\omega_z - \psi), \quad (4)$$

respectively. The anti-symmetric part is defined by the difference between the macrorotation ω_z and the microrotation ψ . For $\omega_z = \psi$, the relative strains reduce to their classical definitions (Barber, 2010), for example, $\varepsilon_{xy} = u'_y - \omega_z = (u'_y + \phi)/2$.

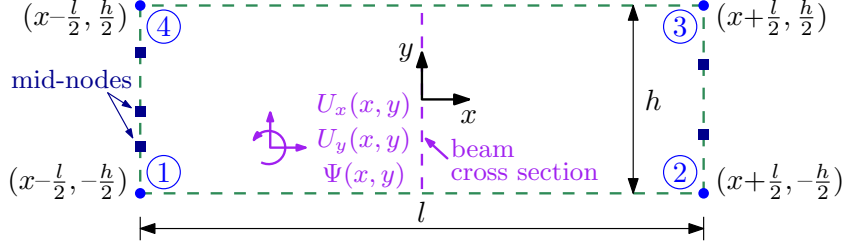


Figure 1: Arbitrary cross section of the micropolar beam possessing microstructure of length l (beam length $\geq l$).

2.2. Two-scale constitutive modeling

Figure 1 shows a rectangular unit cell attached to an arbitrary cross section of a micropolar Timoshenko beam. The unit cell of length l and height h represent the periodic microstructure of the macrostructural beam ($l \leq \text{beam length}$). The unit cell corner displacements in Fig. 1 are expressed in terms of the micropolar cross-sectional displacements U_x and U_y and rotation Ψ . With distance from an arbitrary beam cross section, Taylor series expansions of Eqs. (1) lead to

$$U_x(x \pm l/2, \pm h/2) = u_x \pm \frac{h}{2} \left[\frac{1}{2}(\gamma_s - \gamma_a) - \psi \right] \pm \frac{l}{2} \left(\varepsilon_x^0 \pm \frac{h}{2} \kappa_x \right), \quad (5)$$

$$U_y(x \pm l/2, \pm h/2) = u_y \pm \frac{l}{2} \left[\frac{1}{2}(\gamma_s + \gamma_a) + \psi \right], \quad (6)$$

$$\Psi(x \pm l/2, \pm h/2) = \psi \pm \frac{l}{2} \kappa_{xz}, \quad (7)$$

where the micropolar strains (2)–(4) have been imposed on the cross-sectional rotation ϕ and the displacement gradients. Using the node numbering of Fig. 1, we can write the discrete-to-continuum transformation given by Eqs. (5)–(7) for the corner nodes in matrix form

$$\mathbf{d}^c = \mathbf{T}_u^c \mathbf{u} + \mathbf{T}_\varepsilon^c \boldsymbol{\varepsilon}, \quad (8)$$

where the generalized discrete displacement vector is

$$\mathbf{d}^c = \{U_{x,1} \ U_{y,1} \ \Psi_1 \ U_{x,2} \ U_{y,2} \ \Psi_2 \ U_{x,3} \ U_{y,3} \ \Psi_3 \ U_{x,4} \ U_{y,4} \ \Psi_4\}^T \quad (9)$$

and the vectors for the continuous variables read

$$\mathbf{u} = \{u_x \ u_y \ \phi \ \psi\}^T, \quad (10)$$

$$\boldsymbol{\varepsilon} = \{\varepsilon_x^0 \ \kappa_x \ \gamma_s \ \gamma_a \ \kappa_{xz}\}^T. \quad (11)$$

The transformation matrices \mathbf{T}_u^c and \mathbf{T}_ε^c are given in Appendix A. For additional mid-nodes located at $\pm l/2$ and connected to the neighboring unit cells, a similar transformation can be written as

$$\mathbf{d}^m = \mathbf{T}_u^m \mathbf{u} + \mathbf{T}_\varepsilon^m \boldsymbol{\varepsilon}. \quad (12)$$

The complete discrete-to-continuum transformation reads

$$\mathbf{d} = \begin{Bmatrix} \mathbf{d}^c \\ \mathbf{d}^m \end{Bmatrix} = \begin{bmatrix} \mathbf{T}_u^c & \mathbf{T}_\varepsilon^c \\ \mathbf{T}_u^m & \mathbf{T}_\varepsilon^m \end{bmatrix} \begin{Bmatrix} \mathbf{u} \\ \boldsymbol{\varepsilon} \end{Bmatrix}. \quad (13)$$

The transformation by Eq. (13) for nodes located at the unit cell edges $x = \pm l/2$ may be applied to different finite element based lattice unit cells once static condensation has been applied at all nodes located between $l/2 < x < l/2$. The unit cell can be modeled, for example, by using Euler-Bernoulli or Timoshenko beam finite elements as both choices result in a system that is consistent with the generalized displacement vector (13). As for their material composition, the elements can be heterogeneous and anisotropic. Several lattice cores will be considered in Section 2.3.

The strain energy of a unit cell modeled by beam elements can be written as

$$W = \frac{1}{2} \mathbf{d}^T \mathbf{k} \mathbf{d}, \quad (14)$$

where \mathbf{k} is the global stiffness matrix of the unit cell that corresponds to the master degrees of freedom after the static condensation. It is straightforward to verify that the displacement terms (10) do not contribute to the strain energy of any of the lattice core unit cells considered in this paper and we obtain

$$W = \frac{1}{2} \boldsymbol{\varepsilon}^T \mathbf{T}_\varepsilon^T \mathbf{k} \mathbf{T}_\varepsilon \boldsymbol{\varepsilon}. \quad (15)$$

We define the 1-D density of the unit cell strain energy as

$$W_0^l \equiv \frac{W}{l} = \frac{1}{2} \boldsymbol{\varepsilon}^T \mathbf{C} \boldsymbol{\varepsilon} \quad (16)$$

where the constitutive matrix is given by

$$\mathbf{C} = \frac{1}{l} \mathbf{T}_\varepsilon^T \mathbf{k} \mathbf{T}_\varepsilon. \quad (17)$$

For geometrically nonlinear unit cell analysis in which strains are small but rotations may be moderate, we assume that the constitutive matrix (17) remains the same but the axial normal strain is modified so that the strain vector becomes

$$\hat{\boldsymbol{\varepsilon}} = \{\hat{\varepsilon}_x^0 \quad \kappa_x \quad \gamma_s \quad \gamma_a \quad \kappa_{xz}\}^T. \quad (18)$$

in which the nonlinear von Kármán term is included in

$$\hat{\varepsilon}_x^0 = u'_x + \frac{1}{2} (u'_y)^2. \quad (19)$$

The unit cell represents a *lattice material* of which the micropolar beam is made of. We write the hyperelastic constitutive relations for the geometrically nonlinear micropolar beam continuum as

$$\mathbf{S} \equiv \frac{\partial \hat{W}_0^l}{\partial \hat{\boldsymbol{\varepsilon}}} = \frac{1}{2} \frac{\partial}{\partial \hat{\boldsymbol{\varepsilon}}} \left(\hat{\boldsymbol{\varepsilon}}^T \mathbf{C} \hat{\boldsymbol{\varepsilon}} \right) = \mathbf{C} \hat{\boldsymbol{\varepsilon}}, \quad (20)$$

where \mathbf{S} is now the stress resultant vector of the 1-D micropolar beam and for which the general explicit form considered in this paper is

$$\begin{Bmatrix} N_x \\ M_x \\ Q_s \\ Q_a \\ P_{xz} \end{Bmatrix} = \begin{bmatrix} C_{11} & C_{12} & 0 & 0 & C_{15} \\ C_{12} & C_{22} & 0 & 0 & C_{25} \\ 0 & 0 & C_{33} & C_{34} & 0 \\ 0 & 0 & C_{34} & C_{44} & 0 \\ C_{15} & C_{25} & 0 & 0 & C_{55} \end{bmatrix} \begin{Bmatrix} \hat{\varepsilon}_x^0 \\ \kappa_x \\ \gamma_s \\ \gamma_a \\ \kappa_{xz} \end{Bmatrix}, \quad (21)$$

where N_x is the axial force, M_x and P_{xz} are the bending and couple-stress moments, respectively, and Q_s and Q_a are the symmetric and anti-symmetric shear forces defined as Karttunen et al. (2018b)

$$Q_s = \frac{Q_{xy} + Q_{yx}}{2} \quad \text{and} \quad Q_a = \frac{Q_{xy} - Q_{yx}}{2}, \quad (22)$$

respectively. Note that Eq. (20) implies that the bridging of the two scales, i.e., the macroscale (beam) and the microscale (unit cell), is founded on an assumption of strain energy equivalence between them.

2.3. Modeling of lattice materials

In this section, we consider four different lattice material sandwich beam cores, namely, the web-core studied earlier in the linear context (Karttunen et al., 2018b) and the hexagonal, Y-frame and corrugated cores presented in Fig. 2. All cores are made of steel and are modeled using linearly elastic isotropic nodally-exact Euler-Bernoulli beam finite elements. All unit cell beam constituents have a rectangular cross-section and in this paper the width of all unit cells is 0.05 m.

The web-core is modeled using four Euler-Bernoulli beam elements that can be represented by the dashed lines in Fig. 1. In this case, only the corner node transformation (8) needs to be considered and the application of this in Eq. (14) results in the constitutive equations

$$\begin{Bmatrix} N_x \\ M_x \\ Q_s \\ Q_a \\ P_{xz} \end{Bmatrix} = \begin{bmatrix} 2EA_f & 0 & 0 & 0 & 0 \\ & \frac{EA_f h^2}{2} + \Theta & 0 & 0 & \Theta \\ & & \frac{6EI_f + \Theta}{l^2} & \frac{6EI_f - \Theta}{l^2} & 0 \\ & \text{SYM} & & \frac{6EI_f + \Theta}{l^2} & 0 \\ & & & & 2EI_f + \Theta \end{bmatrix} \begin{Bmatrix} \hat{\epsilon}_x^0 \\ \kappa_x \\ \gamma_s \\ \gamma_a \\ \kappa_{xz} \end{Bmatrix} \quad (23)$$

where

$$\Theta = \frac{3EI_w k_\theta l}{6EI_w + k_\theta h}. \quad (24)$$

In the constitutive matrix, EA_f and EI_f are the axial and bending stiffnesses of the horizontal faces, respectively. For the vertical webs we have EA_w , EI_w and k_θ for the axial, bending and rotational joint stiffnesses, respectively. The webs are modeled using special-purpose Euler-Bernoulli elements with rotational springs at both ends to account for the flexibility of the laser-welded joints (Chen and Lui, 2005; Monforton and Wu, 1963; Romanoff et al., 2007). The numerical values of the core parameters are $E_f = 212$ GPa, $E_w = 200$ GPa, $k_\theta = 2675$ Nm and $\nu = 0.3$ for the face and web Young's moduli, rotational joint stiffness and Poisson ratio, respectively. The face and web thicknesses are $t_f = 3$ mm and $t_w = 4$ mm, respectively. The height, i.e., the distance between the face central axes is $h = 43$ mm.

For the other cores displayed in Fig. 2, Young's modulus and Poisson ratio are $E = 210$ GPa and $\nu = 0.3$, respectively. Other relevant parameters are given in Fig. 2. The hexagonal core includes two mid-nodes in addition to the four corner nodes that need to be taken into account essentially to ensure connectivity between neighboring unit cells on the micropolar continuum level. Static condensation is applied at the inner nodes of the unit cell. It is difficult to obtain a meaningful

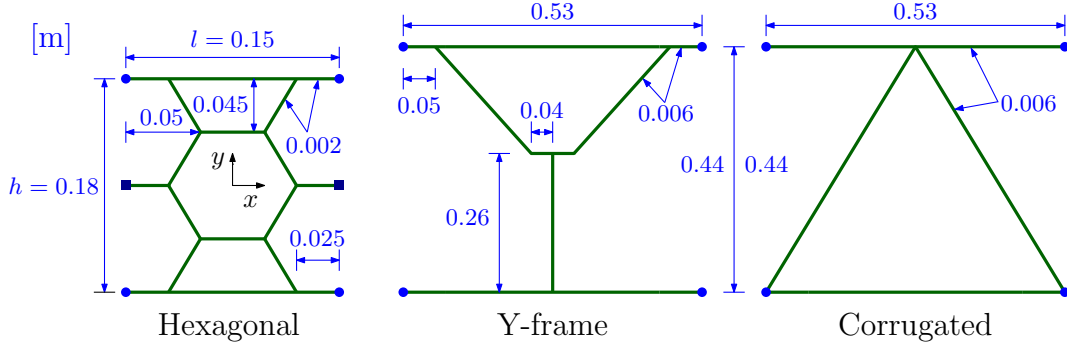


Figure 2: Unit cells of hexagonal, Y-frame and corrugated lattice core sandwich beams. The latter two are modeled according to St-Pierre et al. (2015)

symbolic form for the hexagonal constitutive matrix, in numerical form we have

$$\mathbf{C}_{\text{hex}} = \begin{bmatrix} 4.26438 \cdot 10^7 & 0 & 0 & 0 & 0 \\ 0 & 340740 & 0 & 0 & 27.1761 \\ 0 & 0 & 94735.4 & 8319.08 & 0 \\ 0 & 0 & 8319.08 & 3315.25 & 0 \\ 0 & 27.1761 & 0 & 0 & 44.3467 \end{bmatrix} \quad (25)$$

The constitutive matrix (25) is of the same form as that of the web-core with the exception that for the hexagonal core $C_{33} \neq C_{44}$. For the Y-frame and corrugated cores we obtain

$$\mathbf{C}_Y = \begin{bmatrix} 1.26053 \cdot 10^8 & 11696.2 & 0 & 0 & 5292.50 \\ 11696.2 & 6.10097 \cdot 10^6 & 0 & 0 & 1164.35 \\ 0 & 0 & 42094.9 & 9541.42 & 0 \\ 0 & 0 & 9541.42 & 5302.30 & 0 \\ 5292.50 & 1164.35 & 0 & 0 & 1012.92 \end{bmatrix} \quad (26)$$

and

$$\mathbf{C}_{\text{corr}} = \begin{bmatrix} 1.26018 \cdot 10^8 & -3902.45 & 0 & 0 & -3902.45 \\ -3902.45 & 6.09926 \cdot 10^6 & 0 & 0 & 858.539 \\ 0 & 0 & 2.09792 \cdot 10^7 & 3734.96 & 0 \\ 0 & 0 & 3734.96 & 5078.42 & 0 \\ -3902.45 & 858.539 & 0 & 0 & 1334.05 \end{bmatrix}, \quad (27)$$

respectively. The axial and classical sandwich bending stiffnesses in Eqs. (25)–(27) are practically given by $C_{11} \approx 2EA_f$ and $C_{22} \approx EA_f h^2/2$, respectively. We see that due to the lack of symmetry about the x -axis, the coupling terms C_{12} and C_{15} appear in the constitutive matrices of the Y-frame and corrugated cores. In addition, the symmetric shear stiffness C_{33} of the corrugated core is very high in comparison to that of the other cores because the corrugated lattice core has a stretch-dominated shear-carrying mechanism while the others cores are bending-dominated. In other words, when bent, the constituents of the corrugated lattice core act as axial rods without

significant bending so that the core is very stiff. The differences between bending- and stretch-dominated cores in geometrically nonlinear bending problems will be studied further by numerical examples in Section 4. Finally, it is easy to verify that all eigenvalues of each constitutive matrix above are positive which means that the matrices are positive definite. It follows that each lattice core material is stable in the conventional sense (i.e., strain energy is positive for nonzero strains).

2.4. Geometrically nonlinear beam equations

The principle of virtual displacements can be stated for a geometrically nonlinear micropolar Timoshenko beam as

$$\delta W = \delta W_I - \delta W_E = 0, \quad (28)$$

The virtual strain energy stored in a typical beam element, $\Omega = (x_a, x_b)$, and consistent with the strains used in the previous section, is

$$\begin{aligned} \delta W_I &= \int_V (\sigma_x \delta \hat{\varepsilon}_x + m_{xz} \delta \kappa_{xz} + \tau_{xy} \delta \varepsilon_{xy} + \tau_{yx} \delta \varepsilon_{yx}) dV \\ &= \int_{x_a}^{x_b} [N_x (\delta u'_x + u'_y \delta u'_y) + M_x \delta \phi' + P_{xz} \delta \psi' \\ &\quad + Q_{xy} (\delta u'_y - \delta \psi) + Q_{yx} (\delta \phi + \delta \psi)] dx, \end{aligned} \quad (29)$$

where $\hat{\varepsilon}_x = \hat{\varepsilon}_x^0 + y \kappa_x$ [cf. Eqs. (2) and (19)]. The external virtual work is

$$\delta W_E = \int_{x_a}^{x_b} q \delta u_y dx + \sum_{i=1}^8 Q_i \delta U_i, \quad (30)$$

where $q(x)$ is the distributed transverse load, Q_i are the generalized external forces at the beam ends and U_i are the associated generalized displacements defined as

$$\begin{aligned} U_1 &= u_x(x_a), & U_5 &= u_x(x_b), \\ U_2 &= u_y(x_a), & U_6 &= u_y(x_b), \\ U_3 &= \phi(x_a), & U_7 &= \phi(x_b), \\ U_4 &= -\psi(x_a), & U_8 &= -\psi(x_b). \end{aligned} \quad (31)$$

Equation (28) conforms to the micropolar beam finite element presented in Fig. 3 and provides the weak form for the finite element formulation in Section 3. On the other hand, Eq. (28) yields the Euler-Lagrange equations

$$N'_x = 0, \quad V'_{xy} = -q, \quad Q_{yx} - M'_x = 0, \quad P'_{xz} + Q_{xy} - Q_{yx} = 0, \quad (32)$$

where the effective transverse shear force is

$$V_{xy} = Q_{xy} + N_x u'_y. \quad (33)$$

Finally, when the corresponding generalized displacements are not defined, the natural (or force) boundary conditions become

$$\begin{aligned} Q_1 &= -N_x(x_a), & Q_5 &= N_x(x_b), \\ Q_2 &= -V_{xy}(x_a), & Q_6 &= V_{xy}(x_b), \\ Q_3 &= -M_x(x_a), & Q_7 &= M_x(x_b), \\ Q_4 &= P_{xz}(x_a), & Q_8 &= -P_{xz}(x_b). \end{aligned} \quad (34)$$

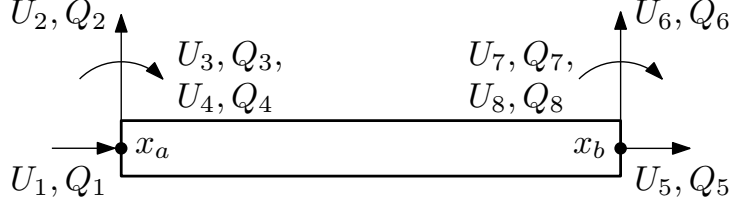


Figure 3: Set-up according to which the micropolar Timoshenko beam finite element will be developed in Section 3.

The equilibrium equations (32) may be presented in terms of displacements by using the constitutive relations (21). The governing equations could also have been derived by employing the principle of minimum total potential energy and the strain energy density \hat{W}_0^l given in Eq. (20).

3. Geometrically nonlinear micropolar Timoshenko beam element

3.1. Finite element formulation

The finite element model is developed using the statement of the principle of virtual displacements (28) over a typical element $\Omega^e = (x_a, x_b)$, which takes the explicit form

$$0 = \int_{x_a}^{x_b} \{ N_x(\delta u'_x + u'_y \delta u'_y) + M_x \delta \phi' + P_{xz} \delta \psi' + Q_{xy}(\delta u'_y - \delta \psi) + Q_{yx}(\delta \phi + \delta \psi) \} dx - \int_{x_a}^{x_b} q \delta u_y dx - \sum_{i=1}^8 Q_i \delta U_i \quad (35)$$

After using the constitutive equations in (21), the following four statements for a typical finite element $\Omega^e = (x_a, x_b)$ which are equivalent to Eq. (35) can be written

$$0 = \int_{x_a}^{x_b} \left\{ C_{11} \left(u'_x + \frac{1}{2} (u'_y)^2 \right) + C_{12} \phi' + C_{15} \psi' \right\} \delta u'_x dx - Q_1 \delta U_1 - Q_5 \delta U_5 \quad (36)$$

$$0 = \int_{x_a}^{x_b} \left\{ \left(\left[C_{11} \left(u'_x + \frac{1}{2} (u'_y)^2 \right) + C_{12} \phi' + C_{15} \psi' \right] u'_y \right) \delta u'_y + ((C_{33} + C_{34})(u'_y + \phi) + (C_{34} + C_{44})(u'_y - \phi - 2\psi)) \delta u'_y \right\} dx - \int_{x_a}^{x_b} q \delta u_y dx - Q_2 \delta U_2 - Q_6 \delta U_6 \quad (37)$$

$$0 = \int_{x_a}^{x_b} \left\{ \left(C_{12} \left(u'_x + \frac{1}{2} (u'_y)^2 \right) + C_{22} \phi' + C_{25} \psi' \right) \delta \phi' + ((C_{33} - C_{34})(u'_y + \phi) + (C_{34} - C_{44})(u'_y - \phi - 2\psi)) \delta \phi \right\} dx - Q_3 \delta U_3 - Q_7 \delta U_7 \quad (38)$$

$$\begin{aligned}
0 = \int_{x_a}^{x_b} & \left\{ \left(C_{15} \left(u'_x + \frac{1}{2} (u'_y)^2 \right) + C_{25}\phi' + C_{55}\psi' \right) \delta\psi' \right. \\
& - 2 \left(C_{34}(u'_y + \phi) + C_{44}(u'_y - \phi - 2\psi) \right) \delta\psi \\
& \left. - Q_4\delta U_4 - Q_8\delta U_8 \right\} dx
\end{aligned} \tag{39}$$

The primary variables are u_x, u_y, ϕ and ψ . These variables are approximated using Lagrange interpolation functions $L_j^{(J)}$, ($J = 1, 2, 3, 4$) (see, for example, Reddy (2019)) so that

$$\begin{aligned}
u_x &\approx \sum_{j=1}^2 u_j L_j^{(1)}(x), & u_y &\approx \sum_{j=1}^2 v_j L_j^{(2)}(x) \\
\phi &\approx \sum_{j=1}^2 \phi_j L_j^{(3)}(x), & \psi &\approx \sum_{j=1}^2 \psi_j L_j^{(4)}(x)
\end{aligned} \tag{40}$$

By substituting Eq. (40) for u_x, u_y, ϕ and ψ and putting $\delta u_x = L_j^{(1)}, \delta u_y = L_j^{(2)}, \delta\phi = L_j^{(3)}$ and $\delta\psi = L_j^{(4)}$ into the weak-form statements in Eqs. (36)–(39), the finite element equations for a typical beam element can be expressed as

$$\begin{bmatrix} \mathbf{K}^{11} & \mathbf{K}^{12} & \mathbf{K}^{13} & \mathbf{K}^{14} \\ \mathbf{K}^{21} & \mathbf{K}^{22} & \mathbf{K}^{23} & \mathbf{K}^{24} \\ \mathbf{K}^{31} & \mathbf{K}^{32} & \mathbf{K}^{33} & \mathbf{K}^{34} \\ \mathbf{K}^{41} & \mathbf{K}^{42} & \mathbf{K}^{43} & \mathbf{K}^{44} \end{bmatrix}^{(e)} \begin{Bmatrix} \mathbf{u}_x \\ \mathbf{u}_y \\ \phi \\ \psi \end{Bmatrix}^{(e)} = \begin{Bmatrix} \mathbf{F}^1 \\ \mathbf{F}^2 \\ \mathbf{F}^3 \\ \mathbf{F}^4 \end{Bmatrix}^{(e)} \tag{41}$$

The stiffness coefficients $K_{ij}^{\alpha\beta}$ and force coefficients F_i^α ($\alpha, \beta = 1, 2, 3, 4$ and $i, j = 1, 2$) are defined as

$$\begin{aligned}
K_{ij}^{11} &= \int_{x_a}^{x_b} \left\{ C_{11} \frac{dL_i^{(1)}}{dx} \frac{dL_j^{(1)}}{dx} \right\} dx \\
K_{ij}^{12} &= \frac{1}{2} \int_{x_a}^{x_b} \left\{ C_{11} \left(\frac{du_y}{dx} \right) \frac{dL_i^{(1)}}{dx} \frac{dL_j^{(2)}}{dx} \right\} dx \\
K_{ij}^{13} &= \int_{x_a}^{x_b} \left\{ C_{12} \frac{dL_i^{(1)}}{dx} \frac{dL_j^{(3)}}{dx} \right\} dx \\
K_{ij}^{14} &= \int_{x_a}^{x_b} \left\{ C_{15} \frac{dL_i^{(1)}}{dx} \frac{dL_j^{(4)}}{dx} \right\} dx \\
K_{ij}^{21} &= \int_{x_a}^{x_b} \left\{ C_{11} \left(\frac{du_y}{dx} \right) \frac{dL_i^{(2)}}{dx} \frac{dL_j^{(1)}}{dx} \right\} dx
\end{aligned}$$

$$\begin{aligned}
K_{ij}^{22} &= \frac{1}{2} \int_{x_a}^{x_b} \left\{ C_{11} \left(\frac{du_y}{dx} \right)^2 \frac{dL_i^{(2)}}{dx} \frac{dL_j^{(2)}}{dx} \right\} dx + \int_{x_a}^{x_b} \left\{ (C_{33} + 2C_{34} + C_{44}) \frac{dL_i^{(2)}}{dx} \frac{dL_j^{(2)}}{dx} \right\} dx \\
K_{ij}^{23} &= \int_{x_a}^{x_b} \left\{ C_{12} \left(\frac{du_y}{dx} \right) \frac{dL_i^{(2)}}{dx} \frac{dL_j^{(3)}}{dx} \right\} dx + \int_{x_a}^{x_b} \left\{ (C_{33} - C_{44}) \frac{dL_i^{(2)}}{dx} L_j^{(3)} \right\} dx \\
K_{ij}^{24} &= \int_{x_a}^{x_b} \left\{ C_{15} \left(\frac{du_y}{dx} \right) \frac{dL_i^{(2)}}{dx} \frac{dL_j^{(4)}}{dx} \right\} dx - 2 \int_{x_a}^{x_b} \left\{ (C_{34} + C_{44}) \frac{dL_i^{(2)}}{dx} L_j^{(4)} \right\} dx \\
K_{ij}^{31} &= \int_{x_a}^{x_b} \left\{ C_{12} \frac{dL_i^{(3)}}{dx} \frac{dL_j^{(1)}}{dx} \right\} dx \\
K_{ij}^{32} &= \frac{1}{2} \int_{x_a}^{x_b} \left\{ C_{12} \left(\frac{du_y}{dx} \right) \frac{dL_i^{(3)}}{dx} \frac{dL_j^{(2)}}{dx} \right\} dx + \int_{x_a}^{x_b} \left\{ (C_{33} - C_{44}) L_i^{(3)} \frac{dL_j^{(2)}}{dx} \right\} dx \\
K_{ij}^{33} &= \int_{x_a}^{x_b} \left\{ C_{22} \frac{dL_i^{(3)}}{dx} \frac{dL_j^{(3)}}{dx} \right\} dx + \int_{x_a}^{x_b} \left\{ (C_{33} + C_{44}) L_i^{(3)} L_j^{(3)} \right\} dx \\
K_{ij}^{34} &= \int_{x_a}^{x_b} \left\{ C_{25} \frac{dL_i^{(3)}}{dx} \frac{dL_j^{(4)}}{dx} \right\} dx + 2 \int_{x_a}^{x_b} \left\{ (C_{44} - C_{34}) L_i^{(3)} L_j^{(4)} \right\} dx \\
K_{ij}^{41} &= \int_{x_a}^{x_b} \left\{ C_{15} \frac{dL_i^{(4)}}{dx} \frac{dL_j^{(1)}}{dx} \right\} dx \\
K_{ij}^{42} &= \frac{1}{2} \int_{x_a}^{x_b} \left\{ C_{15} \left(\frac{du_y}{dx} \right) \frac{dL_i^{(4)}}{dx} \frac{dL_j^{(2)}}{dx} \right\} dx - 2 \int_{x_a}^{x_b} \left\{ (C_{34} + C_{44}) L_i^{(4)} \frac{dL_j^{(2)}}{dx} \right\} dx \\
K_{ij}^{43} &= \int_{x_a}^{x_b} \left\{ C_{25} \frac{dL_i^{(4)}}{dx} \frac{dL_j^{(3)}}{dx} \right\} dx - 2 \int_{x_a}^{x_b} \left\{ (C_{34} - C_{44}) L_i^{(4)} L_j^{(3)} \right\} dx \\
K_{ij}^{44} &= \int_{x_a}^{x_b} \left\{ C_{55} \frac{dL_i^{(4)}}{dx} \frac{dL_j^{(4)}}{dx} \right\} dx + 4 \int_{x_a}^{x_b} \left\{ C_{44} L_i^{(4)} L_j^{(4)} \right\} dx
\end{aligned} \tag{42}$$

$$\begin{aligned}
F_i^1 &= Q_1 L_i^{(1)}(x_a) + Q_5 L_i^{(1)}(x_b) \\
F_i^2 &= \int_{x_a}^{x_b} q(x) L_i^{(2)} dx + Q_2 L_i^{(1)}(x_a) + Q_6 L_i^{(1)}(x_b) \\
F_i^3 &= Q_3 L_i^{(1)}(x_a) + Q_7 L_i^{(1)}(x_b) \\
F_i^4 &= Q_4 L_i^{(1)}(x_a) + Q_8 L_i^{(1)}(x_b)
\end{aligned} \tag{43}$$

3.2. Solution of nonlinear equations

The nonlinear finite element equations (41) are solved iteratively using the Newton's iteration procedure (see Reddy (2015)). The linearized element equation at the beginning of the r^{th} iteration will take the form:

$$\mathbf{T}^{(e)}(\mathbf{U}^{(e)(r-1)}) \Delta \mathbf{U}^{(e)(r)} = -\mathbf{R}^{(e)}(\mathbf{U}^{(e)(r-1)}) \tag{44}$$

Where $\mathbf{U}^{(e)(r-1)}$ is the generalized nodal displacement vector of element e at the end of $(r-1)^{th}$ iteration and $\Delta\mathbf{U}^{(e)(r)}$ is the incremental displacement vector of element e at the r^{th} iteration defined as

$$\mathbf{U}^{(e)(r)} = \mathbf{U}^{(e)(r-1)} + \Delta\mathbf{U}^{(e)(r)} \quad (45)$$

The residual vector $\mathbf{R}^{(e)}(\mathbf{U}^{(e)(r-1)})$, computed after the end of $(r-1)^{th}$ iteration, is defined as

$$\mathbf{R}^{(e)}(\mathbf{U}^{(e)(r-1)}) = \mathbf{K}^{(e)}\mathbf{U}^{(e)(r-1)} - \mathbf{F}^{(e)} \quad (46)$$

Once the residual vector is computed using Eq. (46), the tangent stiffness matrix $\mathbf{T}^{(e)}$ can be calculated using the following definition

$$\mathbf{T}^{(e)} \equiv \frac{\partial \mathbf{R}^{(e)}}{\partial \mathbf{U}^{(e)}} \quad \text{or} \quad T_{ij}^{(e)} = \frac{\partial R_i^{(e)}}{\partial U_j^{(e)}} \quad (47)$$

For a typical element, writing Eq. (44) in a fashion similar to Eq. (41), we get

$$\begin{bmatrix} \mathbf{T}^{11} & \mathbf{T}^{12} & \mathbf{T}^{13} & \mathbf{T}^{14} \\ \mathbf{T}^{21} & \mathbf{T}^{22} & \mathbf{T}^{23} & \mathbf{T}^{24} \\ \mathbf{T}^{31} & \mathbf{T}^{32} & \mathbf{T}^{33} & \mathbf{T}^{34} \\ \mathbf{T}^{41} & \mathbf{T}^{42} & \mathbf{T}^{43} & \mathbf{T}^{44} \end{bmatrix}^{(e)} \begin{bmatrix} \Delta\mathbf{U}^1 \\ \Delta\mathbf{U}^2 \\ \Delta\mathbf{U}^3 \\ \Delta\mathbf{U}^4 \end{bmatrix}^{(e)} = - \begin{bmatrix} \mathbf{R}^1 \\ \mathbf{R}^2 \\ \mathbf{R}^3 \\ \mathbf{R}^4 \end{bmatrix}^{(e)} \quad (48)$$

where the notation $\mathbf{U}^1 = \mathbf{u}_x$, $\mathbf{U}^2 = \mathbf{u}_y$, $\mathbf{U}^3 = \phi$ and $\mathbf{U}^4 = \psi$ is used. Then the coefficients of the tangent stiffness matrix, $T_{ij}^{\alpha\beta}$ ($\alpha, \beta = 1, 2, 3, 4$ and $i, j = 1, 2$), in the above equation can be computed as

$$T_{ij}^{\alpha\beta} = K_{ij}^{\alpha\beta} + \sum_{\gamma=1}^4 \sum_{p=1}^2 \frac{\partial (K_{ip}^{\alpha\gamma})}{\partial U_j^{\beta}} U_p^{\gamma} \quad (49)$$

In explicit terms, the coefficients read

$$T_{ij}^{11} = K_{ij}^{11}, \quad T_{ij}^{12} = K_{ij}^{12} + \frac{1}{2} \int_{x_a}^{x_b} \left\{ C_{11} \frac{du_y}{dx} \frac{dL_i^{(1)}}{dx} \frac{dL_j^{(2)}}{dx} \right\} dx, \quad T_{ij}^{13} = K_{ij}^{13}, \quad T_{ij}^{14} = K_{ij}^{14}, \quad (50)$$

$$T_{ij}^{21} = K_{ij}^{21}, \quad T_{ij}^{23} = K_{ij}^{23}, \quad T_{ij}^{24} = K_{ij}^{24},$$

$$T_{ij}^{31} = K_{ij}^{31}, \quad T_{ij}^{32} = K_{ij}^{32} + \frac{1}{2} \int_{x_a}^{x_b} \left\{ C_{12} \frac{du_y}{dx} \frac{dL_i^{(3)}}{dx} \frac{dL_j^{(2)}}{dx} \right\} dx, \quad T_{ij}^{33} = K_{ij}^{33}, \quad T_{ij}^{34} = K_{ij}^{34},$$

$$T_{ij}^{41} = K_{ij}^{41}, \quad T_{ij}^{42} = K_{ij}^{42} + \frac{1}{2} \int_{x_a}^{x_b} \left\{ C_{15} \frac{du_y}{dx} \frac{dL_i^{(4)}}{dx} \frac{dL_j^{(2)}}{dx} \right\} dx, \quad T_{ij}^{43} = K_{ij}^{43}, \quad T_{ij}^{44} = K_{ij}^{44}, \quad (51)$$

$$\begin{aligned} T_{ij}^{22} = & K_{ij}^{22} + \int_{x_a}^{x_b} \left\{ C_{11} \frac{du_x}{dx} \frac{dL_i^{(2)}}{dx} \frac{dL_j^{(2)}}{dx} \right\} dx + \int_{x_a}^{x_b} \left\{ C_{11} \left(\frac{du_y}{dx} \right)^2 \frac{dL_i^{(2)}}{dx} \frac{dL_j^{(2)}}{dx} \right\} dx \\ & + \int_{x_a}^{x_b} \left\{ C_{12} \frac{d\phi}{dx} \frac{dL_i^{(2)}}{dx} \frac{dL_j^{(2)}}{dx} \right\} dx + \int_{x_a}^{x_b} \left\{ C_{15} \frac{d\psi}{dx} \frac{dL_i^{(2)}}{dx} \frac{dL_j^{(2)}}{dx} \right\} dx \end{aligned}$$

The element equations computed from Eq. (48) are assembled and solved (after the imposition of the boundary conditions) to obtain the global incremental displacement vector $\Delta \mathbf{U}$ at the r^{th} iteration. The normalized difference between solution vectors from two consecutive iterations, measured with Euclidean norm, is computed at the end of each iteration. If the value computed is less than a preselected tolerance ε further iterations are terminated

$$\sqrt{\frac{\Delta \mathbf{U} \cdot \Delta \mathbf{U}}{\mathbf{U}^{(r)} \cdot \mathbf{U}^{(r)}}} = \sqrt{\frac{\sum_{I=1}^N |U_I^{(r)} - U_I^{(r-1)}|^2}{\sum_{I=1}^N |U_I^{(r)}|^2}} \leq \varepsilon \quad (52)$$

Further, acceleration of convergence for some type of nonlinearities may be achieved by using weighted-average of solutions from the last two iterations rather than the solution from the last iteration to evaluate the coefficient matrix:

$$\mathbf{U}^{(r)} = \mathbf{K}(\bar{\mathbf{U}})^{-1} \mathbf{F}(\bar{\mathbf{U}}), \quad \bar{\mathbf{U}} \equiv \beta \mathbf{U}^{(r-2)} + (1 - \beta) \mathbf{U}^{(r-1)}, \quad 0 \leq \beta \leq 1 \quad (53)$$

where β is known as the acceleration parameter. The value of β depends on the nature of nonlinearity and the type of problem considered. Once the convergence is obtained the final solution is computed using

$$\mathbf{U}^{(r)} = \mathbf{U}^{(r-1)} + \Delta \mathbf{U}^{(r)} \quad (54)$$

3.3. Shear and Membrane locking

The finite element model used in this paper uses linear interpolation on both u_y and ϕ . However, in the thin beam limit, when linear interpolation is used for u_y , the cross-sectional rotation ϕ should approach $-(du_y/dx)$, which is necessarily constant. But since ϕ is also interpolated as linear, it can never be constant. This inconsistency causes what is known as shear locking (see Reddy (2015)). To avoid this inconsistency, we may use equal interpolation on both u_y and ϕ but treat ϕ as constant while evaluating the symmetric γ_s and anti-symmetric γ_a shear strains. This amounts to using reduced Gauss quadrature rule in evaluating the integrals containing constants C_{33} , C_{34} and C_{44} while computing the element coefficient matrices of Eq. (41) and Eq. (48).

When von Kármán nonlinearity is included, there is coupling between u_x and u_y which causes the beam to undergo axial displacement even when there are no axial forces. But in the case of hinged-hinged beam, there are no constraints on u_x at the boundaries, thus causing the beam to roll over freely without axial strain, i.e.,

$$\hat{\varepsilon}_x^0 = \frac{du_x}{dx} + \frac{1}{2} \left(\frac{du_y}{dx} \right)^2 = 0$$

In order to satisfy this we need

$$-\frac{du_x}{dx} \sim \left(\frac{du_y}{dx} \right)^2$$

In essence, we need to have the same degree of polynomial variation on both (du_x/dx) and $(du_y/dx)^2$. But when equal interpolation of degree greater than one is used for both u_x and u_y this criteria cannot be satisfied and leads to what is known as membrane locking (see Reddy (2015)). To overcome this we have to treat $(du_y/dx)^2$ as same order as (du_x/dx) . This is achieved using reduced integration while evaluating all the nonlinear terms of the element coefficients matrices of Eqs. (41) and (48).

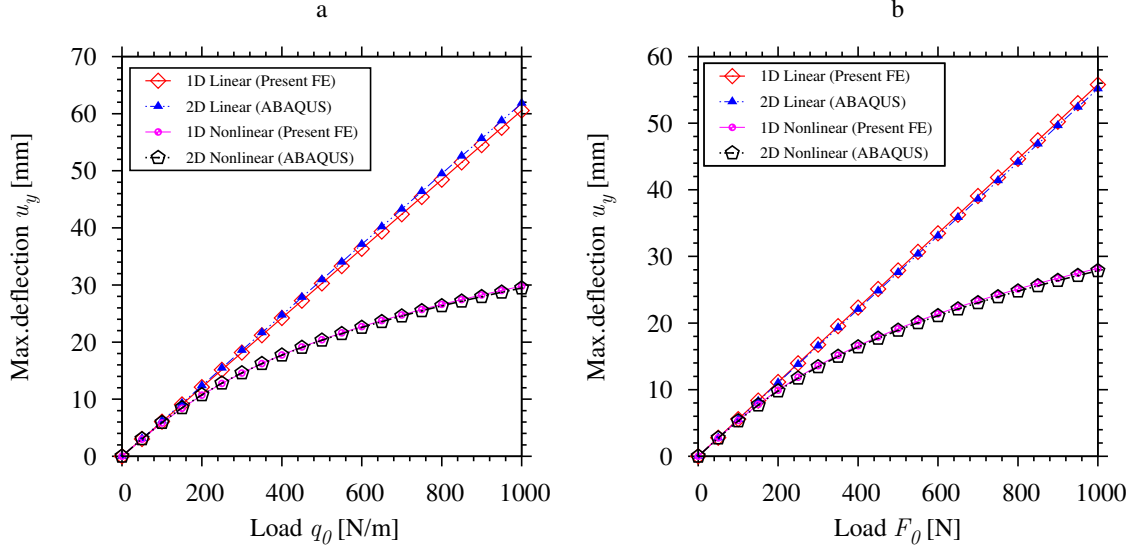


Figure 4: (a) Maximum transverse deflection of a fixed-fixed web-core beam subjected to a uniformly distributed load. (b) Maximum transverse deflection of a web-core beam under three-point-bending.

4. Numerical bending examples

4.1. General Setup

The developed micropolar beam finite element model is used for bending analysis of lattice core sandwich beams. The four structural cores considered in Section 2.3 are used in the calculations. Both geometrically linear and nonlinear cases are analyzed using the 1-D beam model. 2-D reference solutions are computed using Euler–Bernoulli FE beam frames modeled by Abaqus; the pins in simply-supported cases are at the central axis of the 2-D frame so that the model corresponds to 1-D cases.

4.2. Bending of a web-core beam

A beam consisting of 24 web-core unit cells is considered first. The length of each web-core unit cell is $l = 0.12$ m resulting in a total beam length of $L = 2.88$ m. The beam is analyzed for two different boundary conditions, namely, a fixed-fixed case and a three-point-bending setup. For the fixed-fixed case the boundaries are subjected to the following conditions:

$$\begin{aligned} x = 0 : u_x = 0, u_y = 0, \phi = 0, \psi = 0 \\ x = L : u_x = 0, u_y = 0, \phi = 0, \psi = 0 \end{aligned} \quad (55)$$

A uniformly distributed load q_0 is exerted on the beam. The load is applied in increments of $\Delta q_0 = 50$ N/m until a maximum load of 1000 N/m is reached. The maximum deflection, which occurs at the center of the beam, is recorded against the corresponding applied load. The results for both linear and nonlinear cases are plotted in Fig. 4a. The nonlinear deflections are smaller than the linear deflections at large loads because, as the load increases, the internal forces resisting the deformation increase in a nonlinear fashion.

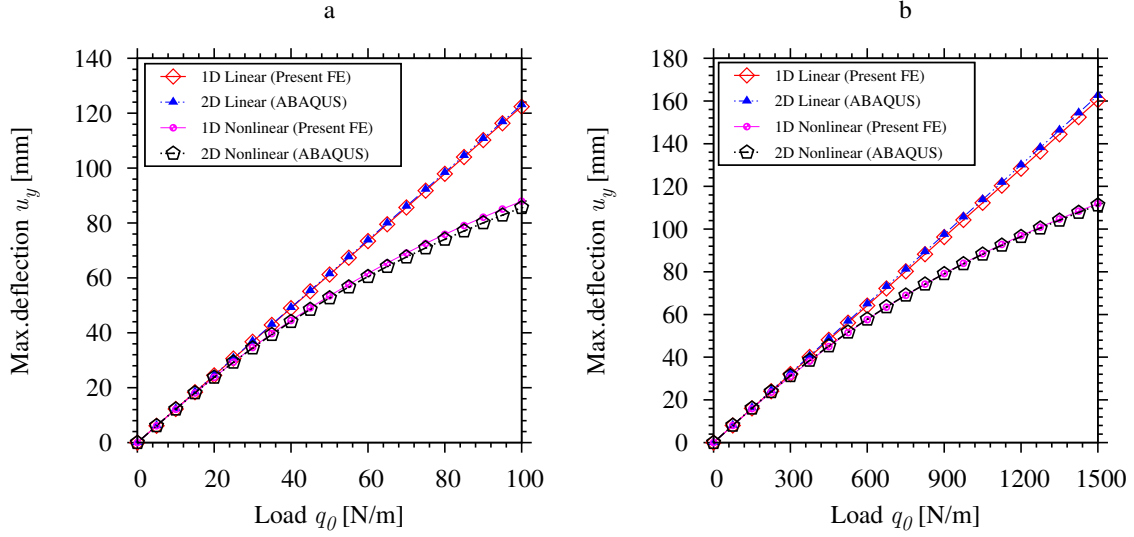


Figure 5: Maximum deflection of a (a) Y-frame and (b) hexagonal core sandwich beams subjected to a uniformly distributed load under fixed-fixed boundary conditions.

For the three-point-bending case the boundaries are subjected to the following conditions:

$$\begin{aligned}
 x = 0 : u_x = 0, u_y = 0, M_x = 0, P_{xz} = 0 \\
 x = L : u_x = 0, u_y = 0, M_x = 0, P_{xz} = 0
 \end{aligned}
 \tag{56}$$

Here, instead of a uniformly distributed load, a point load F_0 is applied at the center of the beam. The point load is applied in increments of $\Delta F_0 = 50$ N until a maximum load of 1000 N is reached. The maximum deflection, which occurs at the center of the beam, is recorded against the corresponding applied load. The results from the finite element model developed here for the 1-D equivalent single layer beam are compared with the 2-D FE results (see Fig. 4b). Note that ABAQUS uses a more complete Green-Lagrange strain tensor for the geometrically nonlinear beam element, whereas in the present finite element model developed in this paper the nonlinearity is included in the form of von Kármán strains.

4.3. Fixed-fixed hexagonal and Y-frame core beams

Here we consider two beams, one made of 48 hexagonal core unit cells and the other made of 30 Y-frame unit cells (see Fig. 2). Thus, the total length of the hexagonal core beam is $L = 7.2$ m and the length of Y-frame core beam is $L = 15.9$ m. Both the beams are subjected to a uniformly distributed load q_0 . Fixed-fixed boundary conditions (55) are applied at the beam ends. For the hexagonal core beam the load is applied in increments of $\Delta q_0 = 75$ N/m until a maximum load of 1500 N/m is reached, while for the Y-frame core beam the load is applied in increments of $\Delta q_0 = 5$ N/m until a maximum load of 100 N/m is reached. The maximum transverse deflections, which occur at the beam centers, are recorded and plotted against the corresponding applied load in Figs. 5a and 5b.

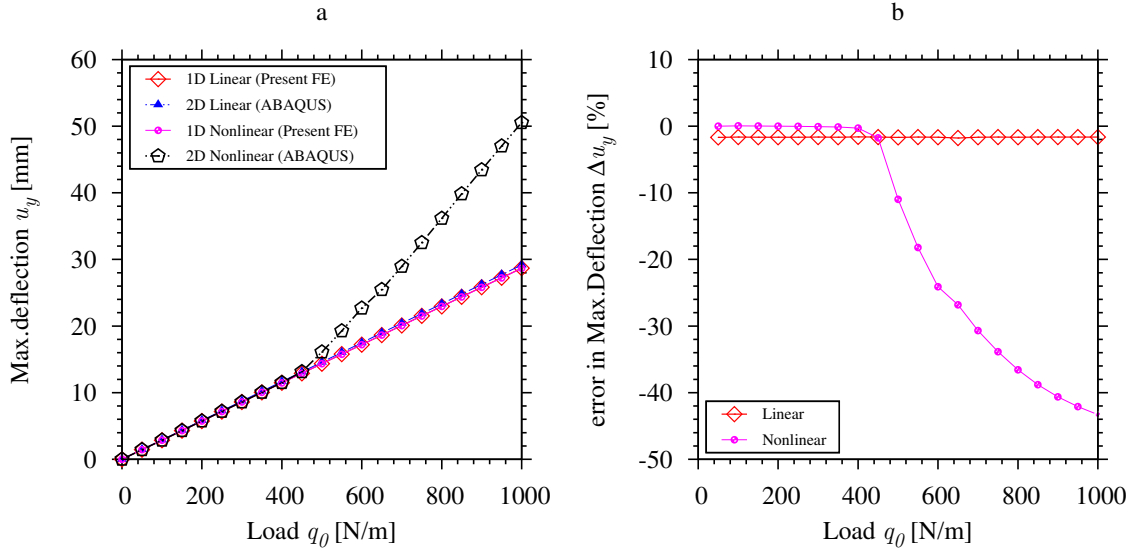


Figure 6: (a) Maximum deflection of a corrugated core sandwich beam subjected a uniformly distributed load under fixed-fixed boundary conditions. Local buckling occurs in the 2-D reference model near $q = 500$ N/m which cannot be accounted for by the micropolar 1-D model. (b) Percentage error of 1D beam model developed, in terms of maximum vertical deflection relative to 2D-beam frame solution (face sheet deflection) calculated using ABAQUS.

4.4. Fixed-fixed corrugated core beam

A beam consisting of 30 corrugated core unit cells is considered. Since the length of each corrugated unit cell is $l = 0.53$ m, the total length of the beam is $L = 15.9$ m (see Fig. 2). The beam is subjected to fixed-fixed boundary conditions (55). A uniformly distributed load q_0 is applied on the beam. The load is applied in increments of $\Delta q_0 = 50$ N/m until a maximum load of 1000 N/m is reached. The maximum vertical deflection of the beam is plotted against the corresponding applied load in Fig. 6a. The error in the maximum vertical deflection is calculated using,

$$\Delta u_y = 100 \times \left(\frac{u_y^{1-D \text{ micropolar}} - u_y^{2-D \text{ beam frame}}}{u_y^{2-D \text{ beam frame}}} \right) \quad (57)$$

and is plotted against the applied load for both the linear and nonlinear cases in Fig. 6b.

Unlike the other structural cores, we see that the nonlinear deflections of the corrugated core beam, calculated using the finite element model developed for the 1-D equivalent single layer beam, are not in good agreement with the 2-D beam frame results all the way. This is due to the local buckling of the stretch-dominated corrugated core that occurs in the 2-D model as displayed in Fig. 7. The presented 1-D equivalent single layer model cannot account for this local buckling.

We also note that even though the lengths and heights of both corrugated core and Y-frame core beams are equal, the corrugated core beam is much stiffer than the Y-frame core beam. The maximum nonlinear deflection for the Y-frame core beam subjected to fixed-fixed boundary conditions is 88 mm at a uniformly distributed load of 100 N/m (see Fig. 5a), while for the corrugated core beam the maximum deflection for a uniformly distributed load of 100 N/m is only 2.9 mm (see Fig. 6a). The high stiffness of the corrugated core beam is attributed to its stretch-dominated behavior unlike Y-frame core which is bending-dominated. The corrugated core has a

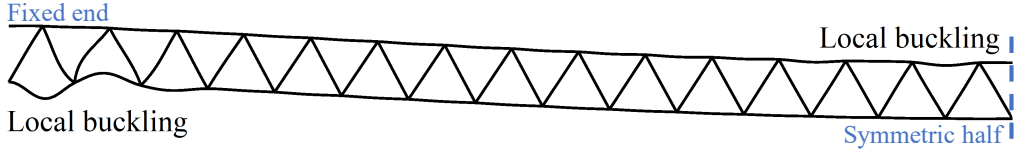


Figure 7: Local buckling of a corrugated core sandwich beam modeled as a 2-D FE beam frame (Abaqus) under a uniformly distributed load $q_0 = 700$ N/m (see Fig. 6 for reference). The 1-D micropolar beam theory takes into account only the global behavior of lattice core beams.

very high shear stiffness because of the fact that the elements (the Euler-Bernoulli beam elements within the core structure) of the corrugated core act essentially like rods and do not bend much, where as this is not the case in the Y-frame core. Although the elements of the part which resemble the corrugated core (the upper ‘V’ part of ‘Y’) in the Y-frame core do not exhibit lot of bending, the remaining part, consisting of lower element, undergoes significant bending.

5. Concluding remarks

In this paper, a displacement-based geometrically nonlinear finite element model for a micropolar Timoshenko beam which can undergo moderate rotations was developed. Appropriate reduced integration techniques were used to prevent the shear and membrane locking of the elements. The beam was used as an equivalent single layer model for lattice core sandwich beams. Constitutive equations were derived for four different lattice cores (hexagonal, corrugated, Y-frame and web-core) using a two-scale energy approach. The global bending results obtained from the developed 1-D finite element model were in good agreement with 2-D beam frame finite element results calculated using the finite element software ABAQUS.

Although the developed model predicts the global deflections with good accuracy, it does not capture the local buckling of stretch-dominated lattice cores. Nevertheless, the model may be extended to local buckling by allowing stiffness reduction inside the microscale unit cells within a computational multiscale finite element framework. Such considerations, and micropolar plates, are left for future studies.

Acknowledgements

The second author acknowledges that this work has received funding from the European Union’s Horizon 2020 research and innovation programme under the Marie Skłodowska–Curie grant agreement No 745770. The financial support is greatly appreciated. The authors also wish to acknowledge CSC – IT Center for Science, Finland, for computational resources (Abaqus usage).

Appendix A. Transformation matrices

The displacement and strain transformation matrices in Eq. (8) are

$$\mathbf{T}_u^c = \begin{bmatrix} 1 & 0 & 0 & 1 & 0 & 0 & 1 & 0 & 0 & 1 & 0 & 0 \\ 0 & 1 & 0 & 0 & 1 & 0 & 0 & 1 & 0 & 0 & 1 & 0 \\ 0 & 0 & 0 & 0 & 0 & 0 & 0 & 0 & 0 & 0 & 0 & 0 \\ \frac{h}{2} & -\frac{l}{2} & 1 & \frac{h}{2} & \frac{l}{2} & 1 & -\frac{h}{2} & \frac{l}{2} & 1 & -\frac{h}{2} & -\frac{l}{2} & 1 \end{bmatrix}^T \quad (\text{A.1})$$

and

$$\mathbf{T}_\varepsilon^c = \begin{bmatrix} -\frac{l}{2} & 0 & 0 & \frac{l}{2} & 0 & 0 & \frac{l}{2} & 0 & 0 & -\frac{l}{2} & 0 & 0 \\ \frac{hl}{4} & 0 & 0 & -\frac{hl}{4} & 0 & 0 & \frac{hl}{4} & 0 & 0 & -\frac{hl}{4} & 0 & 0 \\ -\frac{h}{4} & -\frac{l}{4} & 0 & -\frac{h}{4} & \frac{l}{4} & 0 & \frac{h}{4} & \frac{l}{4} & 0 & \frac{h}{4} & -\frac{l}{4} & 0 \\ \frac{h}{4} & -\frac{l}{4} & 0 & \frac{h}{4} & \frac{l}{4} & 0 & -\frac{h}{4} & \frac{l}{4} & 0 & -\frac{h}{4} & -\frac{l}{4} & 0 \\ 0 & 0 & -\frac{l}{2} & 0 & 0 & \frac{l}{2} & 0 & 0 & \frac{l}{2} & 0 & 0 & -\frac{l}{2} \end{bmatrix}^T \quad (\text{A.2})$$

respectively.

References

References

- Abrate, S., Di Sciuva, M., 2017. Equivalent single layer theories for composite and sandwich structures: A review. *Compos. Struct.*, 179, 482–494.
- Allen, H. G., 1969. *Analysis and Design of Structural Sandwich Panels*. Pergamon Press.
- Ansari, R., Norouzzadeh, A., Shakouri, A. H., Bazdid-Vahdati, M., Rouhi, H., 2018. Finite element analysis of vibrating micro-beams and -plates using a three-dimensional micropolar element. *Thin-Walled Struct.*, 124, 489–500.
- Ansari, R., Shakouri, A. H., Bazdid-Vahdati, M., Norouzzadeh, A., H., R., 2016. A nonclassical finite element approach for the nonlinear analysis of micropolar plates. *J. Comput. Nonlin. Dyn.*, 12 (1).
- Barber, J. R., 2010. *Elasticity*, 3rd Edition. Springer, New York.
- Barut, A., Madenci, E., Anderson, T., Tessler, A., 2002. Equivalent single-layer theory for a complete stress field in sandwich panels under arbitrarily distributed loading. *Compos. Struct.*, 58 (4), 483–495.
- Barut, A., Madenci, E., Heinrich, J., Tessler, A., 2001. Analysis of thick sandwich construction by 3,2-order theory. *Int. J. Solids Struct.*, 38 (34–35), 6063–6077.
- Birman, V., Kardomateas, G. A., 2018. Review of current trends in research and applications of sandwich structures. *Compos. Part B-Eng.*.
- Bitzer, T. N., 1994. Honeycomb marine applications. *J. Reinf. Plast. Compos.*, 13, 355–360.
- Bright, S. R., Smith, J. W., 2004. Fatigue performance of laser-welded steel bridge decks. *Struct. Eng.*, 82 (21).
- Bright, S. R., Smith, J. W., 2007. A new design for steel bridge decks using laser fabrication. *Struct. Eng.*, 85 (21).
- Briscoe, C. R., Mantell, S. C., Davidson, J. H., Okazaki, T., 2011. Design procedure for web core sandwich panels for residential roofs. *J. Sandw. Struct. Mater.*, 13 (1), 23–58.
- Carrera, E., Brischetto, S., 2009. A survey with numerical assessment of classical and refined theories for the analysis of sandwich plates. *Appl. Mech. Rev.*, 62 (1), 010803.
- Chen, W. H., Lui, E. M., 2005. *Handbook of Structural Engineering*. CRC Press.
- Davalos, J. F., Qiao, P., Xu, X. F., Robin, J., Barth, K. E., 2001. Modeling and characterization of fiber-reinforced plastic honeycomb sandwich panels for highway bridge applications. *Compos. Struct.*, 52, 441–452.
- Ding, N., Xu, X., Zheng, Z., 2016. A size-dependent nonlinear microbeam model based on the micropolar elasticity theory. *Acta Mech.* 227 (12), 3497–3515.
- Eringen, A. C., Suhubi, E. S., 1964. Nonlinear theory of simple micro-elastic solids, i and ii. *Int. J. Eng. Sci.*, 2 (2), 189–203.
- Godio, M., Stefanou, I., Sab, K., Sulem, J., 2014. Dynamic finite element formulation for cosserat elastic plates. *Int. J. Numer. Meth. Eng.*, 101 (3).
- Hassanpour, S., Heppler, G., 2014. Uncomplicated torsion and bending theories for micropolar elastic beams. In *Proceedings of the 11th World Congress on Computational Mechanics*.
- Hohe, J., Librescu, L., 2004. Advances in the structural modeling of elastic sandwich panels. *Mech. Adv. Mater. Struct.*, 11 (4–5), 395–424.
- Huang, F.-Y., Yan, B.-H., Yan, J.-L., Yang, D.-U., 2000. Bending analysis of micropolar elastic beam using a 3-d finite element method. *Int. J. Eng. Sci.*, 38 (3), 275–286.
- Karlsson, K. F., Åström, B. T., 1997. Manufacturing and applications of structural sandwich components. *Compos. Part A-Appl. S.*, 28 (2), 97–111.
- Karttunen, A. T., Reddy, J. N., Romanoff, J., 2018a. Micropolar modeling approach for periodic sandwich beams. *Compos. Struct.*, 185, 656–664.

- Karttunen, A. T., Reddy, J. N., Romanoff, J., 2018b. Two-scale constitutive modeling of a lattice core sandwich beam. *Compos. Part B-Eng.*, In Press, <https://doi.org/10.1016/j.compositesb.2018.09.098>.
- Knox, E. M., Cowling, M. J., Winkle, I. E., 1998. Adhesively bonded steel corrugated core sandwich construction for marine applications. *Mar. Struct.*, 11 (4–5), 185–204.
- Kujala, P., Klanac, A., 2005. Steel sandwich panels in marine applications. *Brodogradnja* 56 (4), 305–314.
- Li, L., Xie, S., 2004. Finite element method for linear micropolar elasticity and numerical study of some scale effects phenomena in mems. *Int. J. Mech. Sci.*, 46 (11), 1571–1587.
- Monforton, G. R., Wu, T. H., 1963. Matrix analysis of semi-rigid connected frames. *J. Struct. Div-ASCE* 89 (6), 13–24.
- Mouritz, A. P., Gellert, E., Burchhill, P., Challis, K., 2001. Review of advanced composite structures for naval ships and submarines. *Compos. Struct.*, 53, 21–41.
- Nilsson, P., Al-Emrani, M., Atashipour, S. R., 2017. Transverse shear stiffness of corrugated core steel sandwich panels with dual weld lines. *Thin Wall. Struct.*, 117, 98–112.
- Noor, A. K., Burton, W. S., 1995. Assessment of computational models for sandwich panels and shells. *Comp. Method App. M.*,s 124 (1-2), 125–151.
- Pothier, A., Rencis, J. J., 1994. Three-dimensional finite element formulation for microelastic solids. *Comput. Struct.* 51 (1), 1–21.
- Reddy, J. N., 2004. *Mechanics of Laminated Composite Plates and Shells: Theory and Analysis*, 2nd Edition. CRC Press, Boca Raton, FL.
- Reddy, J. N., 2015. *An Introduction to Nonlinear Finite Element Analysis*, 2nd Edition. Oxford University Press, Oxford, UK.
- Reddy, J. N., 2019. *An Introduction to the Finite Element Method*, 4th Edition. McGraw-Hill, New York, NY.
- Regueiro, R. A., Duan, Z., 2015. Static and dynamic micropolar linear elastic beam finite element formulation, implementation, and analysis. *J. Eng. Mech.*, 141 (8).
- Roland, F., Metschkow, B., 1997. Laser welded sandwich panels for shipbuilding and structural steel engineering. *Transactions on the Built Environment*, vol 24. WIT Press.
- Roman, K., Steinberg, L., 2013. Numerical modeling of bending of micropolar plates. *Thin-Walled Structures* 69, 67–78.
- Romanoff, J., Remes, H., Socha, G., Jutila, M., Varsta, P., 2007. The stiffness of laser stake welded T-joints in web-core sandwich structures. *Thin Wall. Struct.* 45 (4), 453–462.
- Sayyad, A. S., Ghugal, Y. M., 2017. Bending, buckling and free vibration of laminated composite and sandwich beams: A critical review of literature. *Compos. Struct.* 171, 486–504.
- Schwingel, D., Seeliger, H. W., Vecchionacci, C., Alwes, D., Dittrich, J., 2007. Aluminium foam sandwich structures for space applications. *Acta Astronautica*, 61 (1–6), 326–330.
- Skvortsov, v., Bozhevolnaya, E., 2001. Two-dimensional analysis of shallow sandwich panels. *Compos. Struct.* 53 (1), 43–53.
- St-Pierre, L., Fleck, N. A., Deshpande, V. S., 2015. The dynamic indentation response of sandwich panels with a corrugated or Y-frame core. *Int. J. Mech. Sci.* 92, 279–289.
- Vinson, J. R., 1999. *The Behaviour of Sandwich Structures of Isotropic and Composite Materials*. CRC Press.
- Vinson, J. R., 2001. Sandwich structures. *Appl. Mech. Rev.* 54 (3).
- Wadley, H. N. G., Fleck, N. A., Evans, A. G., 2003. Fabrication and structural performance of periodic cellular metal sandwich structures. *Key. Eng. Mater.* 63 (16), 2331–2343.
- Zhou, X., Cusatis, G., 2015. Tetrahedral finite element with rotational degrees of freedom for cosserat and cauchy continuum problems. *J. Eng. Mech.* 141 (2).